We are IntechOpen,
the world's leading publisher of
Open Access books
Built by scientists, for scientists

4,800
Open access books available

122,000
International authors and editors

135M
Downloads

Our authors are among the

154
Countries delivered to

TOP 1%
most cited scientists

12.2%
Contributors from top 500 universities

CLARIVATE ANALYTICS
BOOK CITATION INDEX
INDEXED

WEB OF SCIENCE™

Selection of our books indexed in the Book Citation Index
in Web of Science™ Core Collection (BKCI)

Interested in publishing with us?
Contact book.department@intechopen.com

Numbers displayed above are based on latest data collected.
For more information visit www.intechopen.com

4

Bluff Body Aerodynamics and Wake Control

Efstathios Konstantinidis and Demetri Bouris
Department of Mechanical Engineering
University of Western Macedonia
Bakola & Sialvera, Kozani
Greece

1. Introduction

In aerodynamics, a bluff body is one which has a length in the flow direction close or equal to that perpendicular to the flow direction. This spawns the characteristic that the contribution of skin friction is much lower than that of pressure to the integrated force acting on the body. Even a streamlined body such as an airfoil behaves much like a bluff body at large angles of incidence. A circular cylinder is a paradigm often employed for studying bluff body flows.

Bluff body flows are characterized by flow separation which produces a region of disturbed flow behind, i.e. the wake. Within the near-wake various forms of flow instabilities, both convective and absolute, may be triggered and amplified. These instabilities are manifested by the generation of two- and three-dimensional unsteady flow structures and eventually turbulence as the Reynolds number ($Re = U_\infty D/\nu$, where U_∞ is the incident flow velocity, D is the width of the body and ν is the kinematic viscosity of the fluid) is progressively increased. The most well-known instability is that leading to the periodic formation and shedding of spanwise vortices which produce an impressive wake pattern named after von Kármán and Benhard. The frequency of vortex shedding is characterized by the Strouhal number,

$$St = \frac{f_{vs}D}{U_\infty} \qquad (1)$$

which is a function of the Reynolds number, $St(Re)$. The self-sustained wake oscillations associated with vortex shedding are incited through a Hopf bifurcation as predicted from linearized stability theory (Triantafyllou et al., 1987) and remain in tact over a wide range of Reynolds numbers from approximately 50 to 10^6 or even higher.

Bluff body flows involve the interaction of three shear layers, namely the boundary layer, the separating free shear layers and the wake. The physics of vortex formation and the near-wake flow have been the subject of many past experimental and numerical studies which have provided a wealth of information. The reader is referred to Bearman (1997) for a pertinent review. The basic mechanism of vortex formation is essentially two dimensional although there are inherent three-dimensional features for Reynolds numbers above 190. As well as contributing to time-averaged aerodynamic forces, vortex shedding is responsible for the generation of fluctuating forces acting on the body. This has several ramifications in practical applications as it may excite flow-induced vibration and acoustic noise.

In order to modify the aerodynamic characteristics of bluff bodies, e.g., for control of drag, vibration and noise, it is imperative to control the separated flow in the wake and the

dynamics of vortex formation which are the sources of the fluid forces on the body. Such control can be achieved by both active and passive methods. In active control, it is typical to perturb the wake flow by some sort of excitation mechanism, e.g., rectilinear or rotational oscillations of the body, flow and/or sound forcing, fluid injection and/or blowing (synthetic jets), etc. Some of these methods affect the local flow while others influence the flow globally. The frequency and amplitude of the imposed perturbations provide a means to achieve the desired objective. Passive control is achieved by modification of the cylinder's geometry, e.g., by the addition of tabs, strakes or bumps; these mainly influence the three-dimensional flow characteristics.

A main characteristic of the wake response to periodic perturbations is the 'vortex lock-on' phenomenon whereby the imposed perturbation takes over control of the vortex formation and shedding over a range of conditions in the amplitude–frequency parameter space. For excitation along the flow direction, lock-on occurs when the driving frequency is near twice that of vortex shedding whereas the perturbations need be near the vortex shedding frequency for perturbations transverse to the flow direction. Lock-on is accompanied by a resonant amplification of both mean and fluctuating forces acting on the body but other types of wake response can take place, e.g., different modes of vortex formation can be incited such as symmetric (Konstantinidis & Balabani, 2007). These interactions provide a means for wake flow control.

This chapter presents issues related to the fluid dynamics of bluff bodies in steady and time-dependent flows. The importance of vortex shedding for the generation of aerodynamic forces is exemplified with reference to numerical simulations of two-dimensional fluid flow about a circular cylinder at low Reynolds numbers. Results are presented for the flow patterns in the near-wake and fluid-induced forces exerted on the cylinder in response to flows with superimposed harmonic and non-harmonic perturbations in velocity. Implications for wake control are also discussed. It seems reasonable to concentrate on the stable range of Reynolds number (laminar wake regime) where the effects of simple changes can be studied without the complications attending the presence of turbulent flow.

2. Methodology

In order to study the fluid flow about a circular cylinder and derive the aerodynamic loading, the Navier–Stokes (N–S) equations are solved numerically using a finite volume method on an orthogonal curvilinear grid in two dimensions (2D). The orthogonal curvilinear grid is an appropriate choice for the description of the flow geometry because it can be readily adapted to the cylinder surface while reducing numerical diffusion without introducing overly complex terms in the equations as is the case of general curvilinear or unstructured grids. The governing equations can be written as

$$
\frac{\partial}{\partial t}(\rho\Phi) + \frac{1}{l_\xi l_\eta}\frac{\partial}{\partial \xi}(\rho u l_\eta \Phi) + \frac{1}{l_\xi l_\eta}\frac{\partial}{\partial \eta}(\rho v l_\xi \Phi) =
$$
$$
\frac{1}{l_\xi l_\eta}\frac{\partial}{\partial \xi}(\mu \frac{l_\eta}{l_\xi}\frac{\partial \Phi}{\partial \xi}) + \frac{1}{l_\xi l_\eta}\frac{\partial}{\partial \eta}(\mu \frac{l_\xi}{l_\eta}\frac{\partial \Phi}{\partial \eta}) + S_\Phi
$$
(2)

where ρ and μ is the density and viscosity of the fluid, respectively, l_ξ and l_η are the spatially varying metric coefficients related to the orthogonal curvilinear coordinates (ξ, η), and (u, v) the corresponding velocities in local coordinates. The variable $\Phi = 1, u, v$ for the continuity and momentum equations, respectively, and S_Φ are the source terms, including pressure

terms. The source term is zero for the continuity equation, whereas

$$S_u = -\frac{1}{l_\xi}\frac{\partial p}{\partial \xi} - \frac{\rho uv}{l_\xi l_\eta}\frac{\partial l_\xi}{\partial \eta} + \frac{\rho v^2}{l_\xi l_\eta}\frac{\partial l_\eta}{\partial \xi} + \frac{1}{l_\xi l_\eta}\frac{\partial}{\partial \xi}\left[\frac{l_\eta}{l_\xi}\mu\left(\frac{\partial u}{\partial \xi} + \frac{2v}{l_\eta}\frac{\partial l_\xi}{\partial \eta}\right)\right] +$$
$$\frac{1}{l_\xi l_\eta}\frac{\partial}{\partial \eta}\left[l_\xi \mu\left(\frac{1}{l_\xi}\frac{\partial v}{\partial \xi} - \frac{v}{l_\xi l_\eta}\frac{\partial l_\eta}{\partial \xi} - \frac{u}{l_\xi l_\eta}\frac{\partial l_\xi}{\partial \eta}\right)\right] + \tag{3}$$
$$\frac{\mu}{l_\xi l_\eta}\left(\frac{1}{l_\xi}\frac{\partial v}{\partial \xi} + \frac{1}{l_\eta}\frac{\partial u}{\partial \eta} - \frac{v}{l_\xi l_\eta}\frac{\partial l_\eta}{\partial \xi} - \frac{u}{l_\xi l_\eta}\frac{\partial l_\xi}{\partial \eta}\right)\frac{\partial l_\xi}{\partial \eta} - \frac{2\mu}{l_\xi l_\eta}\left(\frac{1}{l_\eta}\frac{\partial v}{\partial \eta} + \frac{u}{l_\xi l_\eta}\frac{\partial l_\eta}{\partial \xi}\right)\frac{\partial l_\eta}{\partial \xi}$$

for $\Phi = u$, and

$$S_v = -\frac{1}{l_\eta}\frac{\partial p}{\partial \eta} - \frac{\rho uv}{l_\xi l_\eta}\frac{\partial l_\eta}{\partial \xi} + \frac{\rho u^2}{l_\xi l_\eta}\frac{\partial l_\xi}{\partial \eta} + \frac{1}{l_\xi l_\eta}\frac{\partial}{\partial \eta}\left[\frac{l_\xi}{l_\eta}\mu\left(\frac{\partial v}{\partial \eta} + \frac{2u}{l_\xi}\frac{\partial l_\eta}{\partial \xi}\right)\right] +$$
$$\frac{1}{l_\xi l_\eta}\frac{\partial}{\partial \xi}\left[l_\eta \mu\left(\frac{1}{l_\eta}\frac{\partial u}{\partial \eta} - \frac{v}{l_\xi l_\eta}\frac{\partial l_\eta}{\partial \xi} - \frac{u}{l_\xi l_\eta}\frac{\partial l_\xi}{\partial \eta}\right)\right] + \tag{4}$$
$$\frac{\mu}{l_\xi l_\eta}\left(\frac{1}{l_\xi}\frac{\partial v}{\partial \xi} + \frac{1}{l_\eta}\frac{\partial u}{\partial \eta} - \frac{v}{l_\xi l_\eta}\frac{\partial l_\eta}{\partial \xi} - \frac{u}{l_\xi l_\eta}\frac{\partial l_\xi}{\partial \eta}\right)\frac{\partial l_\eta}{\partial \xi} - \frac{2\mu}{l_\xi l_\eta}\left(\frac{1}{l_\xi}\frac{\partial u}{\partial \xi} + \frac{v}{l_\xi l_\eta}\frac{\partial l_\xi}{\partial \eta}\right)\frac{\partial l_\xi}{\partial \eta}$$

for $\Phi = v$. Volume averaging is performed in physical space and the metric coefficients are replaced by the physical distances. All variables are collocated at the grid cell centers so the original SIMPLE algorithm is combined with the Rhie and Chow modification to avoid checker board oscillations in the pressure coupling (Rhie & Chow, 1983). A fully-implicit first-order Euler discretization of the temporal term is used while for the convection and diffusion terms, a higher-order bounded upwind scheme (Papadakis & Bergeles, 1995) and central differencing is employed, respectively.

The grid is initially constructed for half the cylinder and then symmetrically duplicated so that the solid cylinder body is comprised of a number of grid cells defined by two subsequent grid lines in the ξ direction and a number of grid lines in the η direction. Velocity and pressure are artificially set to zero at these cells and they are treated as solid boundaries (no-slip condition) by all neighboring cells. At the lower and upper boundaries of the domain, symmetry conditions are employed. A steady or time-dependent velocity specified at the inlet of the flow domain whereas a convective boundary condition is employed at the outlet in order to avoid backward reflection of pressure waves. The computational domain is rectangular and extends $10D$ upstream, $25D$ downstream and $10D$ above and below the cylinder. The orthogonal curvilinear mesh consists of 299×208 nodes, which is sufficient for mesh-independent results. A time step of the order of $\delta t U_\infty / D = 10^{-2}$ is employed in the simulations. The system of discretized equations is solved using a Tri-Diagonal Matrix Algorithm (TDMA) with an iterative Alternating Direction Implicit (ADI) method.

The sectional forces acting on the cylinder are calculated from the integration of skin friction and pressure around its periphery as

$$F_X = \int_0^{2\pi} \tau_w \sin\theta d\theta + \int_0^{2\pi} p \cos\theta d\theta \tag{5}$$

$$F_Y = \int_0^{2\pi} \tau_w \cos\theta d\theta - \int_0^{2\pi} p \sin\theta d\theta \tag{6}$$

(a) Drag history   (b) Lift history
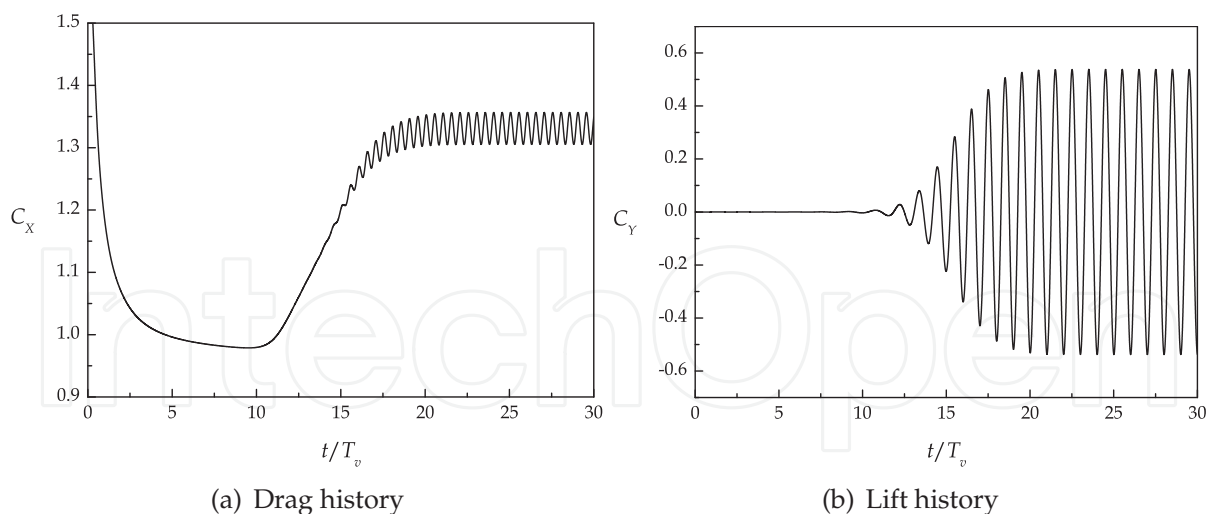
Fig. 1. Instantaneous in-line (drag) and transverse (lift) forces for $Re = 150$.

where θ is the angle measured clockwise from the front stagnation point. The force is nondimensionalized to yield the in-line (drag) and transverse (lift) force coefficients according to formulae

$$C_X = \frac{F_X}{\frac{1}{2}\rho U_\infty^2 D} \quad \text{and} \quad C_Y = \frac{F_Y}{\frac{1}{2}\rho U_\infty^2 D} \tag{7}$$

3. Circular cylinder in steady flow

In this section, results are shown for steady incident flow. The evolution of the instantaneous drag and lift coefficients is shown in Fig. 1 for a typical run at $Re = 150$. In this simulation, the velocity was set to zero everywhere in the flow domain. It takes more than ten periods of vortex shedding for the flow oscillations to be initiated in the wake. During this period, the instantaneous drag drops rapidly from very high values, then reaches a plateau before rising again in Fig. 1(a). Once the instability is triggered, the oscillations are amplified and become saturated in approximately another ten periods as it is seen more clearly in the history of the lift in Fig. 1(b). Beyond this point, a steady-state periodic oscillation is established.

Figure 2 shows the vorticity distribution around the cylinder at six instants over approximately half vortex shedding cycle in the steady periodic state. The instantaneous forces on the cylinder are also shown at the bottom subplots and symbols (red circles) indicate the different instants shown. The figure shows the processes of vortex formation and shedding in the near wake. Vortices are regions of low pressure and as they are formed near the cylinder, a fluctuating pressure field acts on the cylinder surface. As a result, the drag is minimized while a positive vortex (marked by red contour lines) is formed on the bottom side of the cylinder in phases 1 and 2. Subsequently, this positive vortex moves towards the opposite side and away from the cylinder and the drag increases to its maximum in phase 4. In phases 5 and 6, a negative vortex begins to form on the top side of the cylinder which, in turn, will induce a low back pressure and a minimum in drag as it gains strength and size. A maximum in the lift is observed between phases 3 and 4 which is associated with the entrainment of the fluid at the end of the formation region across the wake centreline and towards the top side which causes the negative vortex on the same side to be shed. This process repeats periodically and a staggered vortex street is formed downstream in the wake.
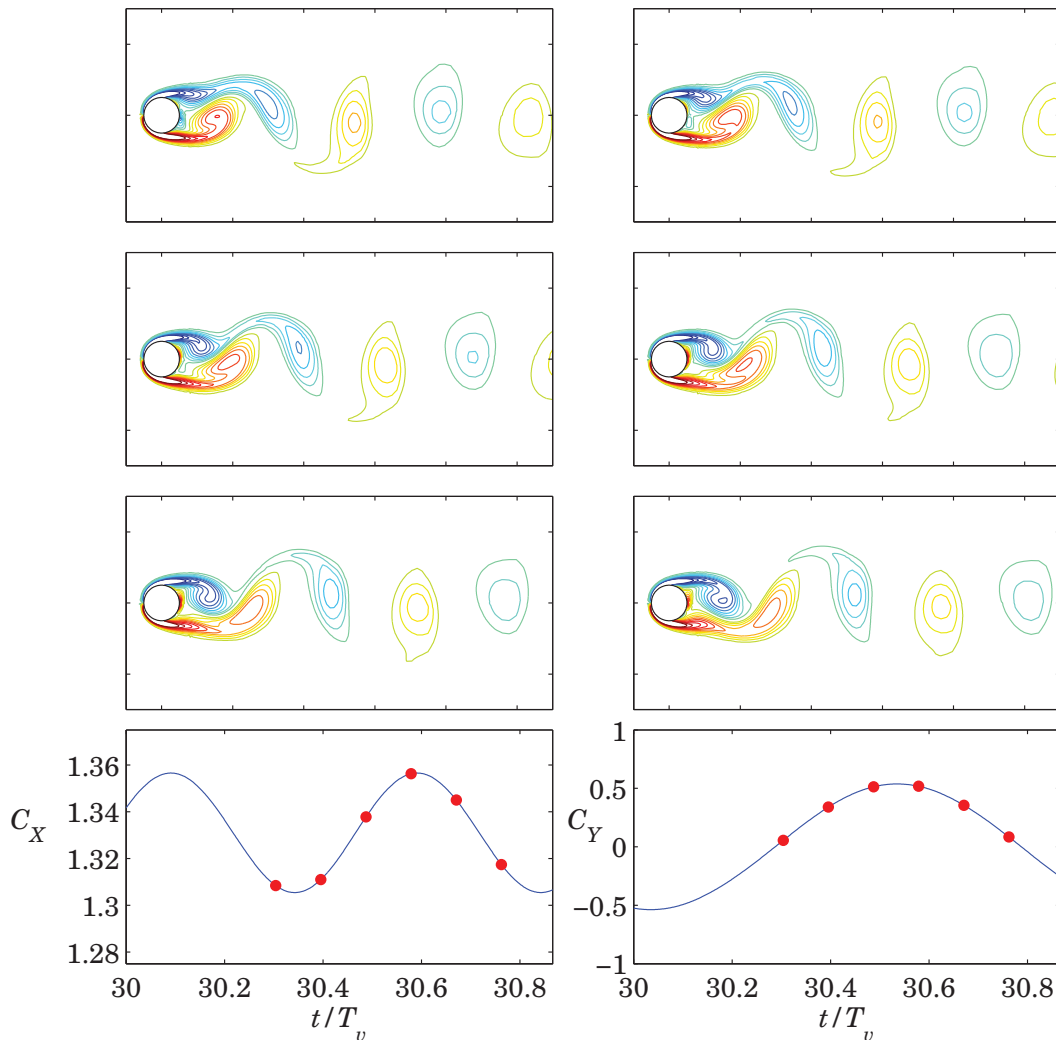
Fig. 2. Vorticity distributions in the cylinder wake and fluid forces on the cylinder at different instants in steady flow; $Re = 150$.

The drag fluctuates at a frequency twice that of the lift since each vortex shed from either side of the cylinder induces a cyclic oscillation in the in-line direction. Hence, the frequency at which vortices are shed from the one side of the cylinder is equal to the frequency of the lift. To some degree of approximation, the instantaneous forces can be represented by harmonic functions

$$C_X(t) = C_D + \sqrt{2}C'_D \sin\left(4\pi f_v t + \phi_D\right), \tag{8}$$

$$C_Y = \sqrt{2}C'_L \sin\left(2\pi f_v t + \phi_L\right). \tag{9}$$

Figure 3 shows some time-averaged statistics of the velocity and pressure fields at $Re = 150$. Velocity is normalized with the incident flow velocity, U_∞, and pressure is normalized with $\frac{1}{2}\rho U_\infty^2$. The distribution of the mean streamwise velocity shows the acceleration of the fluid as it passes over the 'shoulders' of the cylinder and the 'recirculation bubble' (reverse velocities) behind it (Fig. 3(a)). The bubble closure point where the mean velocity becomes zero is located 1.6 diameters behind the cylinder centre. When Bernoulli's equation is applied to the flow

(a) Streamwise mean velocity

(b) Mean pressure

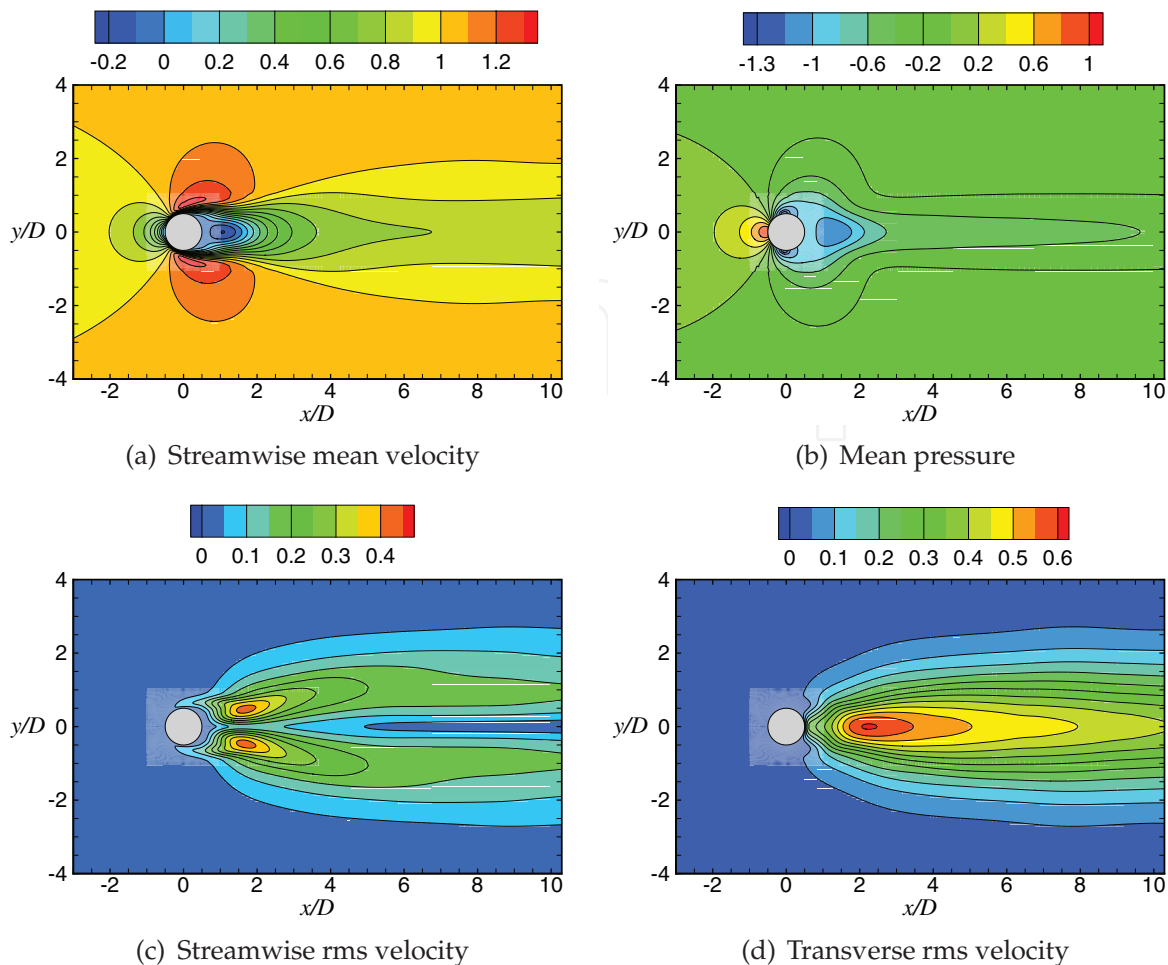(c) Streamwise rms velocity

(d) Transverse rms velocity

Fig. 3. Time-averaged flow characteristics for $Re = 150$.

outside separation, the back pressure coefficient is given by (Griffin & Hall, 1991)

$$C_{pb} = \frac{p_b - p_\infty}{\frac{1}{2}\rho U_\infty^2} = 1 - K^2 \tag{10}$$

where $K = U_s/U_\infty$ is the velocity ratio at separation. The maximum velocity magnitude outside separation is $1.36U_\infty$ at a distance $0.23D$ from the surface. Figure 3(b) shows the distribution of the mean pressure where a back pressure coefficient of $C_{pb} = -0.95$ is obtained, compared to a value of -0.85 computed from the above equation. The mean pressure coefficient attains a minimum value of -1.36 on the surface of the cylinder at $\theta = 85°$ which, coincidently, is exactly equal to the velocity ratio slightly further from the surface. The point of time-averaged flow separation is located at $\theta_s = 112°$. This compares well to the value of $114°$ computed from the following empirical relationship

$$\theta_s = 101.5 + 155.2Re^{-1/2}. \tag{11}$$

The above equation was suggested by Wu et al. (2004) who conducted soap-film experiments and numerical simulations under 2D flow conditions.

	Present study			Henderson (1995)		
Re	C_{Dv}	C_{Dp}	C_D	C_{Dv}	C_{Dp}	C_D
60	0.444	0.985	1.429	0.432	0.984	1.415
90	0.368	0.996	1.364	0.362	0.998	1.360
120	0.323	1.017	1.340	0.319	1.020	1.339
150	0.292	1.040	1.331	0.289	1.044	1.333
180	0.269	1.064	1.334	0.267	1.069	1.336

Table 1. Viscous, pressure and total drag for different Reynolds numbers.

The vortex shedding produces an unsteady flow in the wake that can be characterized by the root-mean-square (rms) magnitude of the velocity fluctuations. Figure 3(c) shows that the streamwise rms velocity exhibits a double-peaked distribution reaching a maximum value of $0.42U_\infty$ at $\{x/D, y/D\} = \{1.67, \pm 0.47\}$. The transverse rms velocity exhibits a single-peaked distribution with a maximum value of $0.60U_\infty$ at $x/D = 2.22$ on the wake centreline as shown in Fig. 3(d). The maxima in the rms velocities are approximately 5% higher than those measured in the cylinder wake at $Re = 2150$ (Konstantinidis & Balabani, 2008). This observation suggests that the mechanism of vortex formation remains basically unaltered over this Re range so long as the boundary layer on the cylinder surface remains laminar until separation.

Simulations were carried out at different Reynolds numbers in the range $Re = 60 - 180$ and the global flow characteristics were determined. One of the key parameters in cylinder wakes is the mean drag coefficient, C_D, which is indicative of the mean energy dissipated in the fluid. Table 1 shows the variation of the mean drag coefficient. The table includes the contribution of the skin friction C_{Dv} and pressure C_{Dp} components to the total force. The skin friction drag reduces monotonically but non-linearly with increasing Reynolds number as might be expected. On the other hand, the pressure drag increases with increasing Reynolds number. As a result, the total drag exhibits a minimum at $Re = 150$. Results are also shown from another numerical study using a high-order spectral element code (Henderson, 1995). The maximum difference of the total drag between the present study and that of Henderson is 1%.

Figure 4 shows the variation of the fluctuating lift coefficient and the Strouhal number as a function of the Reynolds number. Both variables increase as the Reynolds number increases. The solid line in Fig. 4(a) is an empirical fit to experimental data for the sectional lift coefficient provided in Norberg (2003),

$$C_L' = \left(\frac{\epsilon}{30} + \frac{\epsilon^2}{90} \right)^{1/2} \tag{12}$$

where $\epsilon = (Re - 47)/47$. The above equation is valid in the range $Re = 47 - 190$. The present simulations predict a lift coefficient which is slightly above the line representing the empirical relationship. Although small, this difference can be attributed to three-dimensional effects inevitably present in experiments and, in particular, the initiation of slantwise vortex shedding (Gerrard, 1966). Norberg (2003) also provided an empirical relationship for the Strouhal number in the same range $Re = 47 - 190$,

$$St = 0.2663 - 1.019\sqrt{Re}. \tag{13}$$

It should be pointed out that the Strouhal number refers to the frequency at which vortices are shed from one side of the cylinder. The present results agree fairly well with the empirical relationship even though it is based on experimental data.

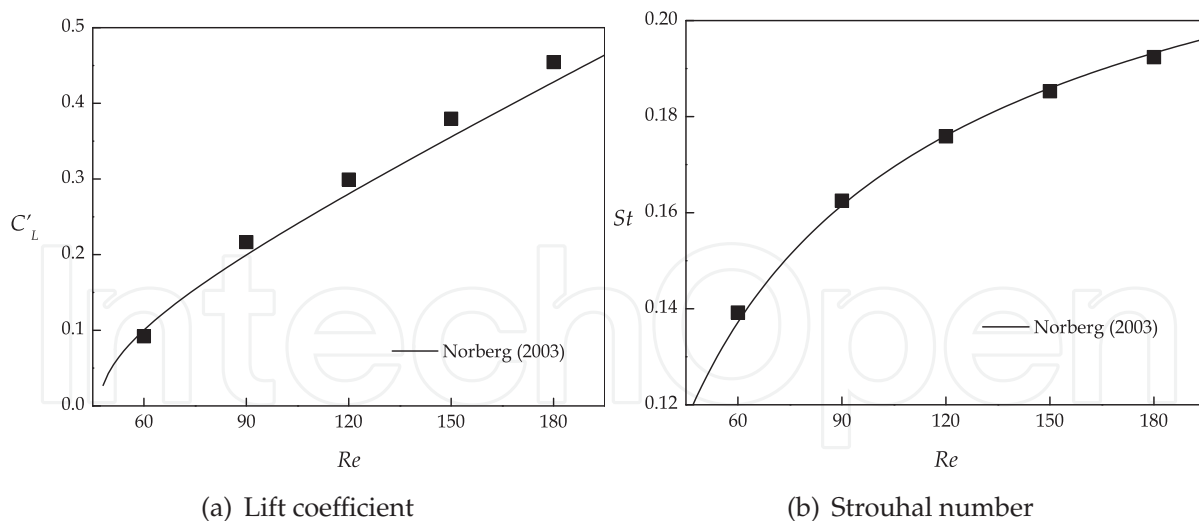(a) Lift coefficient

(b) Strouhal number

Fig. 4. Flow parameters as a function of Reynolds numbers in steady flow. Symbols show the present results while the lines indicate empirical relationships.

Overall, the results presented here for a range of Reynolds numbers in the laminar unsteady wake regime for steady incident flow compare favourably with experimental data and other numerical simulations which provides confidence in the numerical method employed. The simultaneous presentation of the vortex patterns in the wake and fluid forces on the body has revealed effectively the connection between them.

4. Circular cylinder in harmonically perturbed flow

The wake response to harmonic perturbations in the velocity of the incident flow is examined in this section. In this case, two more dimensionless parameters number are required to describe the flow in addition to the Reynolds. The time-depended incident flow velocity is given by

$$U(t) = U_\infty + \Delta u \sin\left(4\pi f_e t\right) \tag{14}$$

where Δu is the amplitude and f_e is the nominal frequency of the imposed velocity perturbations. It should be pointed out that the actual frequency of the velocity waveform in Eq. (14) is $2f_e$ for consistency with non-harmonic waveforms that will be employed in the next section. In the following, the different cases examined will be described in terms of

$$\text{Reduced velocity} = \frac{U_\infty}{f_e D},$$

$$\text{Amplitude ratio} = \frac{\Delta u}{U_\infty}.$$

Results are shown below for a constant Reynolds number ($Re = 150$) and a constant amplitude ratio ($\Delta u/U_\infty = 0.20$). The interest here is in the determination of the vortex lock-on range in which the shedding frequency is captured by the perturbation frequency. For this purpose, a number of runs were conducted starting from perturbation frequencies near the vortex shedding frequency in the unperturbed wake for which lock-on is guaranteed, and either increasing or decreasing the perturbation frequency until the wake response is not locked-on.
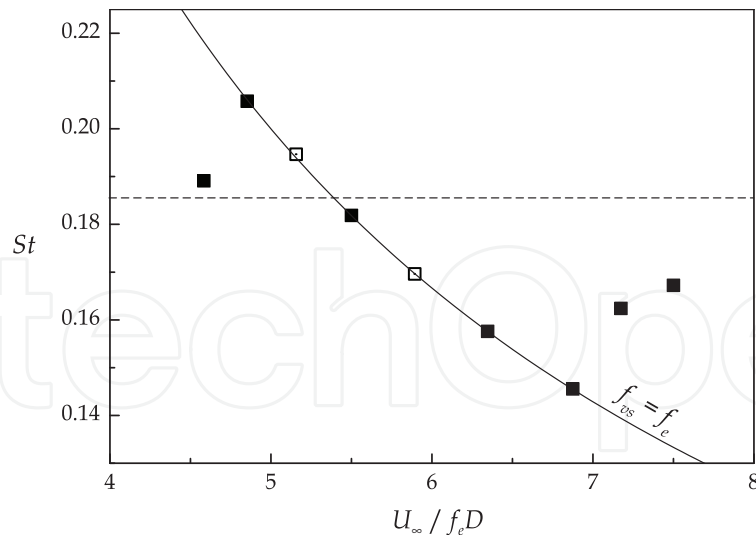
Fig. 5. Variation of the Strouhal number *vs.* reduced velocity.

Figure 5 shows the frequency of vortex shedding in terms of the Strouhal number, $St = f_{vs}D/U_\infty$, as a function of the excitation frequency in terms of the reduced velocity. If there was no interaction between the imposed perturbations and vortex shedding, the Strouhal number would remain constant at the value indicated by a horizontal dashed line. However, the Strouhal number is affected for all the perturbation frequencies considered. For a range of reduced velocities, vortex shedding locks on to the perturbation frequency as indicated by the solid line. For low reduced velocities, the Strouhal number gets higher than its unperturbed value in the natural wake, and vice versa for high reduced velocities. The two cases marked by open symbols will be examined in more detail below.

Figure 6 shows the instantaneous vorticity distributions for two different reduced velocities together with the variation of the drag and lift forces at three instants over approximately half vortex shedding cycle (cf. Fig. 2). For both cases, single vortices are shed alternatively from each side of the cylinder in a fashion similar to that observed for steady flow. However, the details of vortex formation are different. For example, the peak vorticity values and the size of the vortices is increased in harmonically perturbed flow due to wake resonance. Furthermore, the longitudinal distance between shed vortices varies linearly with the reduced velocity. These changes in the wake patterns are accompanied by considerable changes in the magnitude of the mean and fluctuating forces acting on the cylinder. The unsteady in-line force shows a fifty-fold increase in magnitude whereas the transverse increases by 2.5 times compared to their counterparts in steady flow. The in-line force in unsteady flow contains inertial aerodynamic components due to added mass and pressure gradients, i.e.,

$$F_M = \frac{1}{4}\rho\pi D^2 C_M \frac{\mathrm{d}U}{\mathrm{d}t} \tag{15}$$

where $C_M = 1 + C_A$ is the inertia coefficient and C_A the added mass coefficient. Under the conditions examined here, the inertial components of the in-line force dominate over the viscous component. As a consequence, the in-line force is almost in phase with the flow acceleration $\mathrm{d}U/\mathrm{d}t$. On the other hand, the transverse force is not affected by inertial components since there is no perturbation in that direction. In Fig. 6, the waveform of the transverse force deviates markedly from a pure harmonic for both reduced velocities and there is quite a difference between them reflecting the effect of perturbation frequency on C_Y.
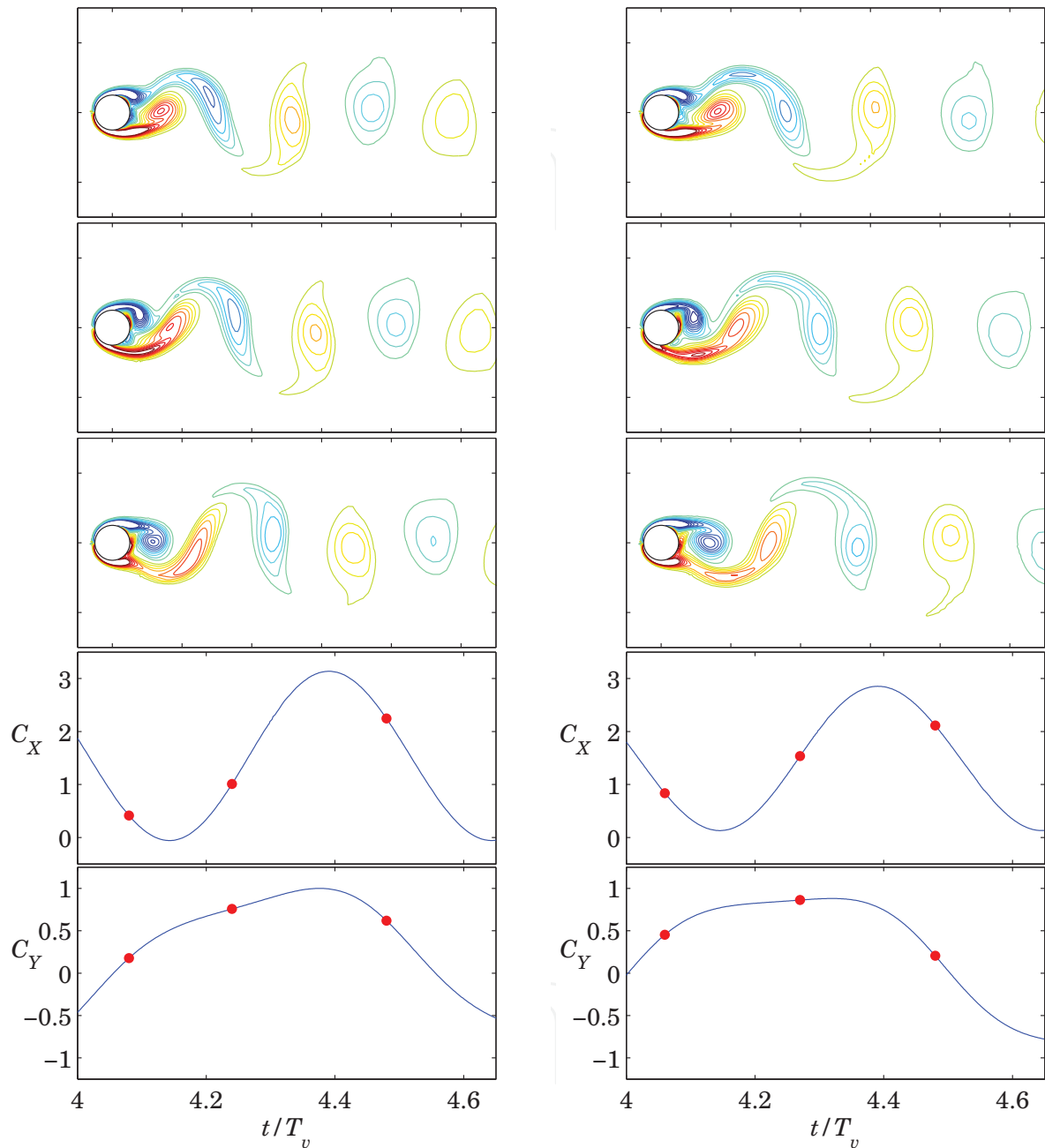
(a) $U_\infty/f_e D = 5.16$

(b) $U_\infty/f_e D = 5.89$

Fig. 6. Vorticity distributions in the cylinder wake and fluid forces on the cylinder at different instants for two reduced velocities in harmonically perturbed flow; $Re = 150$, $\Delta u/U_\infty = 0.20$.
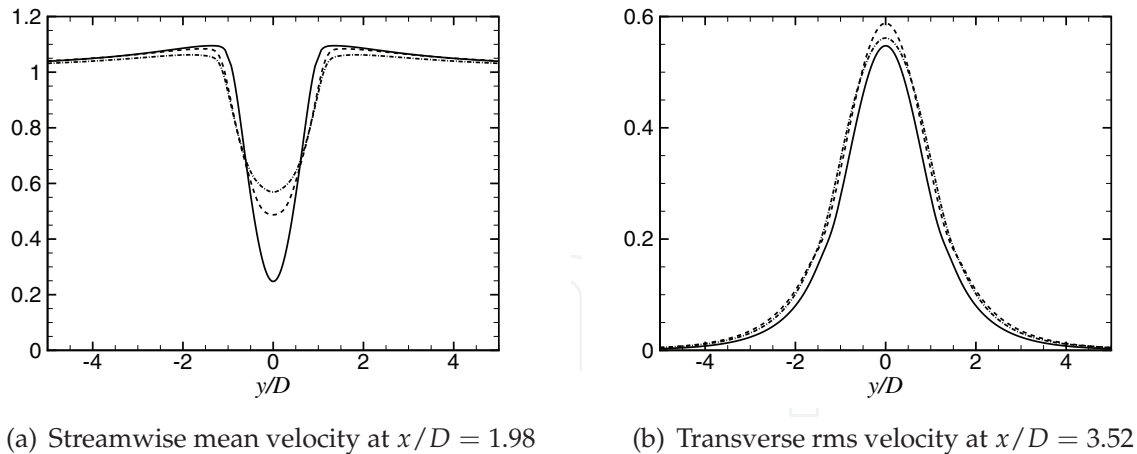
(a) Streamwise mean velocity at $x/D = 1.98$ (b) Transverse rms velocity at $x/D = 3.52$

Fig. 7. Time-averaged flow characteristics for steady and harmonically perturbed incident flow; Solid line: steady flow, dashed line: $U_\infty/f_e D = 5.89$, dash-dot line: $U_\infty/f_e D = 5.16$. All cases: $Re = 150$, $\Delta u/U_\infty = 0.20$.

For $U_\infty/f_e D = 5.89$, the lift attains a very broad maximum which makes it difficult to define precisely the phase, ϕ_L. In other words, the approximation of the lift force as a harmonic function is very crude. Nevertheless, it can be readily verified that the phase at which $C_Y(t)$ is maximum shifts with reduced velocity. E.g., it occurs at $t/T_v \approx 4.4$ for $U_\infty/f_e D = 5.16$ and at a slightly earlier time for $U_\infty/f_e D = 5.89$. In effect, the perturbation frequency provides a means to control the phasing of vortex shedding from the cylinder.

Different perturbation frequencies not only affect the unsteady flow characteristics but also the time-averaged flow. Figure 7 shows the distributions of mean and rms velocities across the wake for two different reduced velocities in harmonically perturbed flow compared to those in steady flow. Clearly, the distributions are much affected in perturbed flow but also depend on the reduced velocity. When looking at the time-averaged location of flow separation it is observed that $\theta_s = 119°$ and $117°$ for $U_\infty/f_e D = 5.16$ and 5.89, respectively. Hence, the separation point moves forward in perturbed flow compared to its location in steady flow.

The variation of the mean drag coefficient over the range of reduced velocities examined for $\Delta u/U_\infty = 0.20$ is shown in Fig. 8. The data show a drag amplification at a reduced velocity of 5.15 reaching a maximum value which is 16% higher than its value for steady flow. Outside lock-on response, the drag coefficient is close to that for the unperturbed flow.

5. Effect of non-harmonic flow perturbations

In this section, the effect of modest deviations of the perturbation waveform from a pure harmonic on the wake flow and fluid forces on the cylinder is examined. The time-depended incident flow velocity is now given by

$$U(t) = \beta \pm \left[1 + \alpha \sin^2(2\pi f_e t)\right]^n \tag{16}$$

where α is a parameter related to the amplitude of velocity perturbations, β sets the mean and median velocity, and the index n dictates the perturbation waveform. For $n = 1$, the waveform is pure-tone harmonic as those employed in the previous section. For $n \neq 1$, the perturbation waveform comprises an infinite number of harmonics. The effect of different values of n has
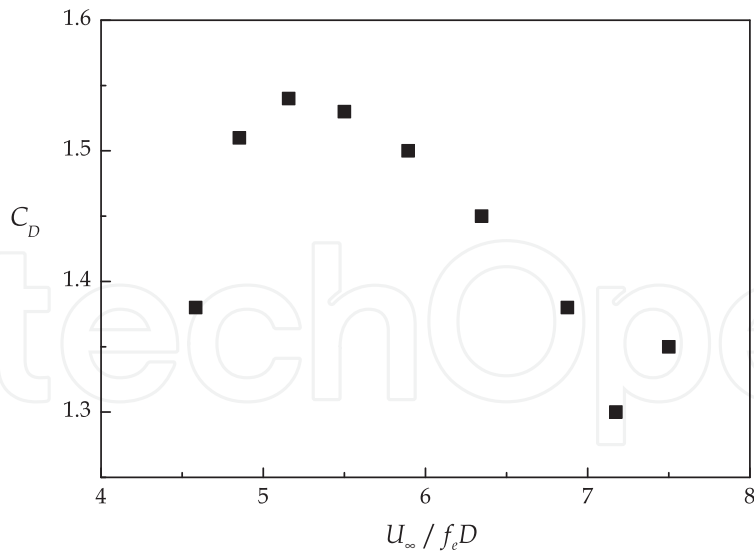
Fig. 8. Variation of the mean drag coefficient *vs.* reduced velocity.

been examined previously by the authors (Konstantinidis & Bouris, 2010). For the present study, a value of $n = -1$ was employed and two different waveforms were produced by using different signs in Eq. (16). Therefore, the waveform produced by a plus sign will be denoted 'plus waveform' and likewise for the 'minus waveform'. The alpha parameter was kept constant so that the velocity amplitude $\Delta U = (U_{max} - U_{min})/2 = 0.20U_\infty$, i.e., the same as that for harmonic perturbations. It should be noted that the time-averaged mean velocity of the incident flow is slightly different for the two different waveforms. Hence, the median velocity $U_0 = (U_{max} + U_{min})/2 \approx U_\infty$ is employed as a reference to allow comparisons. Furthermore, due to the large number of independent variables, results will be shown below only for the two perturbation frequencies which have been examined in more detail in the previous section to allow comparisons between different non-harmonic and harmonic waveforms.

Figure 9 shows the instantaneous vorticity distributions for the two different waveforms together with the drag and lift forces at three instants over approximately half vortex shedding cycle at a reduced velocity of 5.16 (cf. Fig. 2(a)). For both waveforms, the wake response remains phase-locked to the imposed perturbation. Comparison of the vorticity contour lines indicates that the details of vortex formation depend on the perturbation waveform. The plus waveform causes the formation of slightly larger vortices than the minus waveform. Furthermore, the vortices appear to be shed slightly earlier for the minus waveform whereas a plus waveform appears to delay vortex shedding. However, it is difficult to quantify these differences. On the other hand, their effect is more evident on the variation of the fluid forces. The in-line force is markedly different for the two waveforms as it follows the flow acceleration dU/dt due to the dominance of the inertial components. The waveform of the transverse force exhibits some delicate differences, most notably, the time at which it attains its maximum which occurs at a slightly later time for the plus than for the minus waveform. This is consistent with the phasing of vortex shedding above.

Similar observations as those made above concerning the effect of plus and minus waveforms at a reduced velocity of 5.16, also pertain in the case $U_\infty/f_e D = 5.89$ for which results are shown in Fig.10.
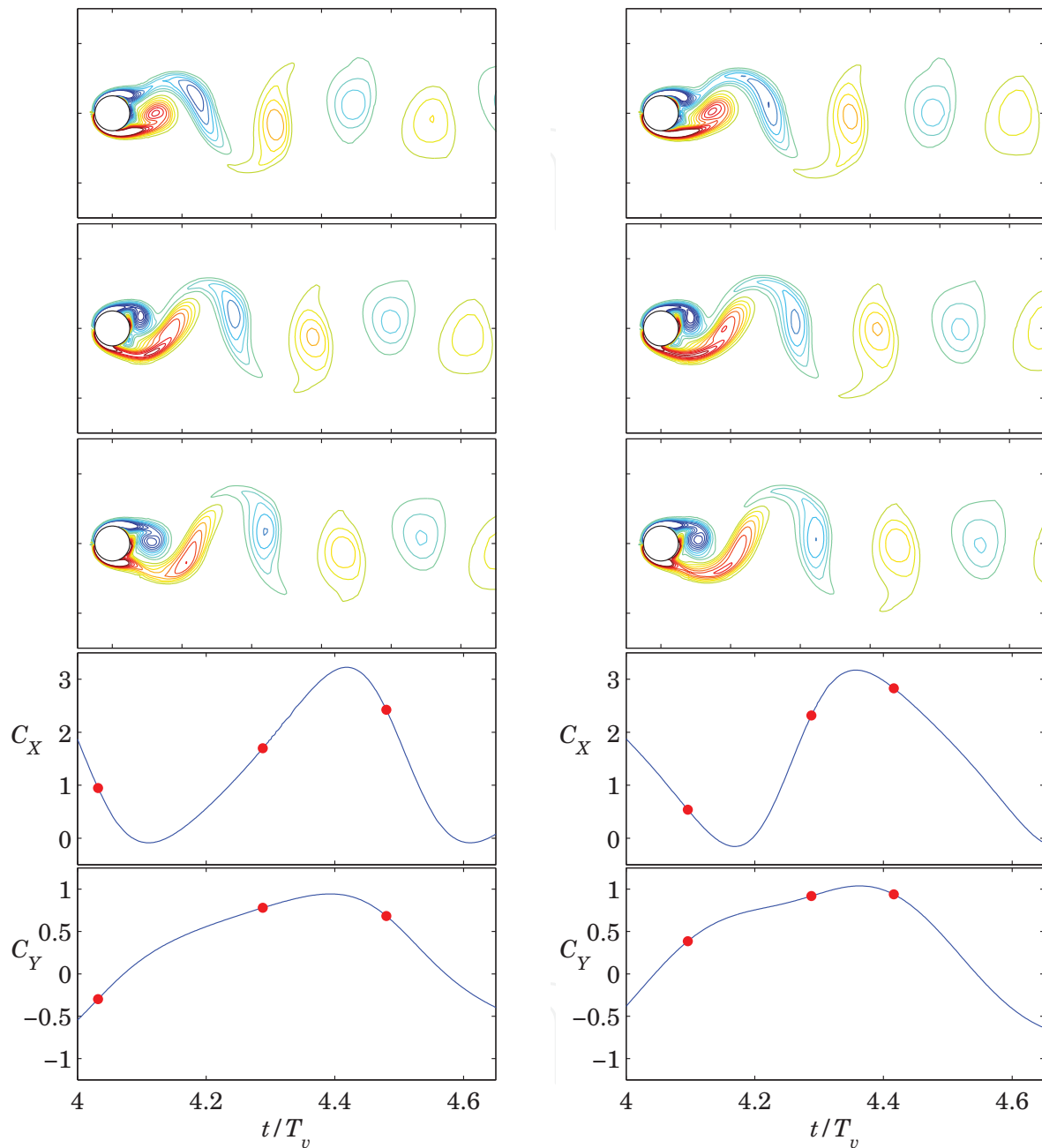
(a) Plus waveform   (b) Minus waveform

Fig. 9. Vorticity distributions in the cylinder wake and fluid forces on the cylinder for two different non-harmonic perturbation waveforms; $U_\infty/f_e D = 5.16$, $\Delta u/U_\infty = 0.20$, $Re \approx 150$.
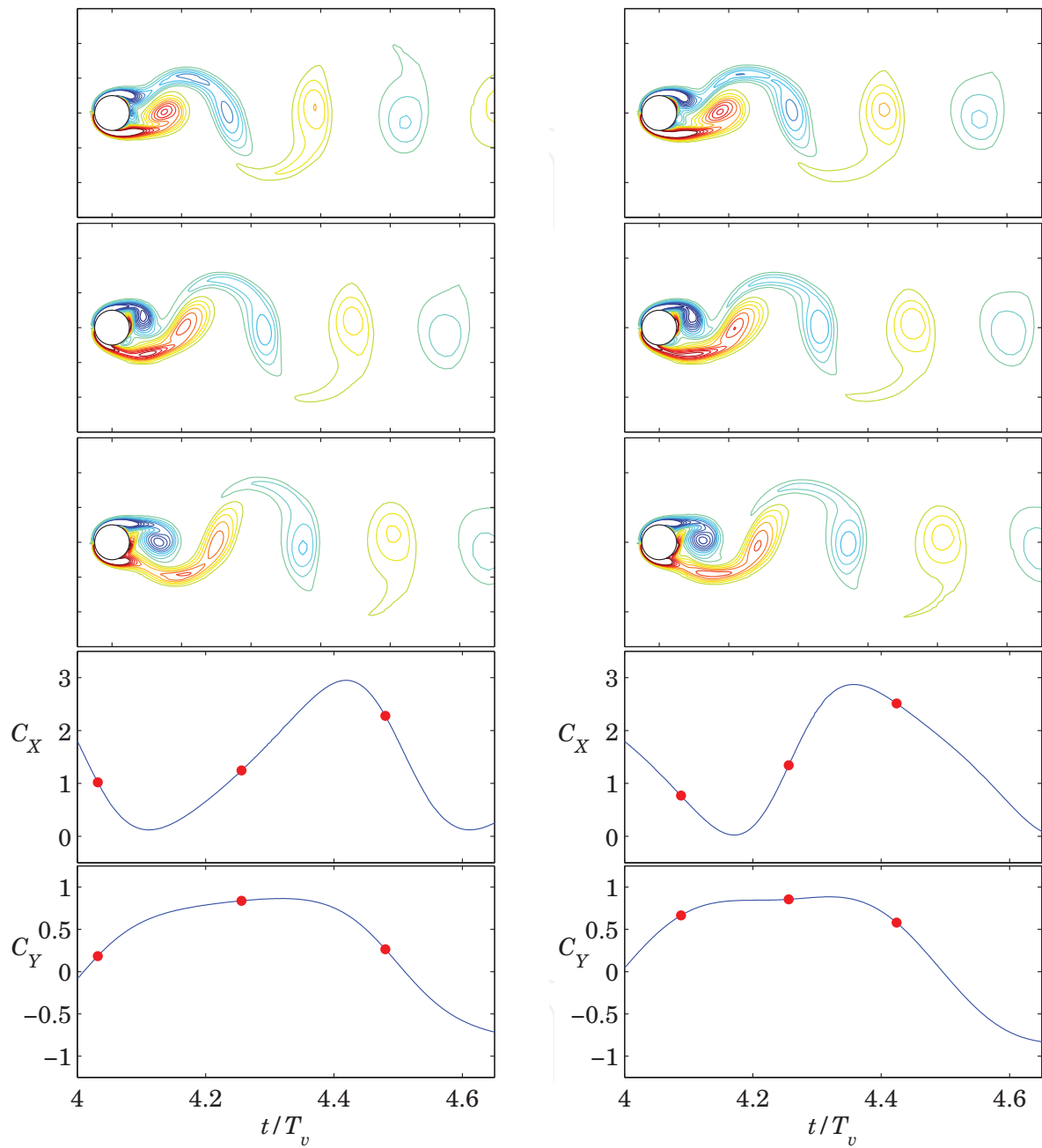
(a) Plus waveform   (b) Minus waveform

Fig. 10. Vorticity distributions in the cylinder wake and fluid forces on the cylinder for two different non-harmonic perturbation waveforms; $U_\infty / f_e D = 5.89$, $\Delta u / U_\infty = 0.20$, $Re \approx 150$.

	Plus waveform		Minus waveform	
$U_\infty / f_e D$	C_D	C_L'	C_D	C_L'
5.16	+3.9	+7.1	-3.9	-4.9
5.89	+2.7	+3.0	-2.0	-1.4

Table 2. Percent difference for two different non-harmonic waveforms compared to the fluid forces calculated for harmonically perturbed flow.

The differences in the time-averaged wake flow are very small for the two non-harmonic waveforms examined and need not be discussed in detail. On the other hand, the time-averaged mean and fluctuating forces reveal the global effect of the perturbation waveform. Table 2 shows the percent change compared to the harmonically perturbed flow for the same reduced velocity and amplitude ratio. The plus waveform causes an increase in the magnitude of both mean drag and rms lift and the opposite happens for the minus waveform. The change is not equivalent for the plus and minus waveform; it is larger for the plus waveform. In addition, these effects are more pronounced for $U_\infty / f_e D = 5.16$ (higher perturbation frequency) than for $U_\infty / f_e D = 5.89$.

6. Conclusion

In this chapter, issues related to the aerodynamics of bluff bodies in steady and time-dependent flows were presented. The subject was treated by numerical simulations of the 2D fluid flow around a circular cylinder which provided information on the dynamics of vortex formation and shedding in the wake and the induced forces acting on the body. Simulations were conducted for low Reynolds numbers in the laminar wake regime, mostly at $Re \approx 150$. Although this approach holds simplifying assumptions compared to real flows of practical interest, the observed phenomena convey over a wide range of Reynolds numbers and, in fact, makes it easier to discern the effects which are otherwise masked by wake turbulence and shear-layer instabilities that develop at higher Reynolds numbers. The results demonstrate that the vortex formation and the wake flow can be controlled by perturbations in the incident flow velocity. This control can be exercised by appropriately selecting the frequency and amplitude of the imposed perturbations on both the mean and fluctuating wake flow and, thereby, on the fluid forces on the cylinder. Whereas harmonic perturbations have been often utilized in the past, the present study also addresses the effect of non-harmonic perturbations, i.e. perturbations whose waveform deviates from a pure-tone harmonic. The findings of the present study illustrate that more effective wake control can be achieved by adjusting the waveform in addition to the perturbation frequency and amplitude.

7. References

Bearman, P. (1997). Near wake flows behind two- and three-dimensional bluff bodies, *Journal of Wind Engineering and Industrial Aerodynamics* Vol. 71: 33–54.

Gerrard, J. H. (1966). The three-dimensional structure of the wake of a circular cylinder, *Journal of Fluid Mechanics* Vol. 25(Part 1): 143–164.

Griffin, O. M. & Hall, M. S. (1991). Vortex shedding lock-on and flow control in bluff body wakes – Review, *Journal of Fluids Engineering* Vol. 113(No. 4): 526–537.

Henderson, R. (1995). Details of the drag curve near the onset of vortex shedding, *Physics of Fluids* Vol. 7(No. 9): 2102–2104.

Konstantinidis, E. & Balabani, S. (2007). Symmetric vortex shedding in the near wake of a circular cylinder due to streamwise perturbations, *Journal of Fluids and Structures* Vol. 23: 1047–1063.

Konstantinidis, E. & Balabani, S. (2008). Flow structure in the locked-on wake of a circular cylinder in pulsating flow: Effect of forcing amplitude, *International Journal of Heat and Fluid Flow* Vol. 29(No. 6): 1567–1576.

Konstantinidis, E. & Bouris, D. (2010). The effect of nonharmonic forcing on bluff-body aerodynamics at a low Reynolds number, *Jouranl of Wind Engineering and Industrial Aerodynamics* Vol. 98: 245–252.

Norberg, C. (2003). Fluctuating lift on a circular cylinder: review and new measurements, *Journal of Fluids and Structures* Vol. 17(No. 1): 57–96.

Papadakis, G. & Bergeles, G. (1995). A locally modified 2nd-order upwind scheme for convection terms discretization, *International Journal of Numerical Methods for Heat and Fluid Flow* Vol. 5(No. 1): 49–62.

Rhie, C. M. & Chow, W. L. (1983). Numerical study of the turbulent - Flow past an airfoil with trailing edge separation, *AIAA Journal* Vol. 21(No. 11): 1525–1532.

Triantafyllou, G., Kupfer, K. & Bers, A. (1987). Absolute instabilities and self-sustained oscillations in the wakes of circular-cylinders, *Physical Review Letters* Vol. 59(No. 17): 1914–1917.

Wu, M. H., Wen, C. Y., Yen, R. H., Weng, M. C. & Wang, A. B. (2004). Experimental and numerical study of the separation angle for flow around a circular cylinder at low Reynolds number, *Journal of Fluid Mechanics* Vol. 515: 233–260.
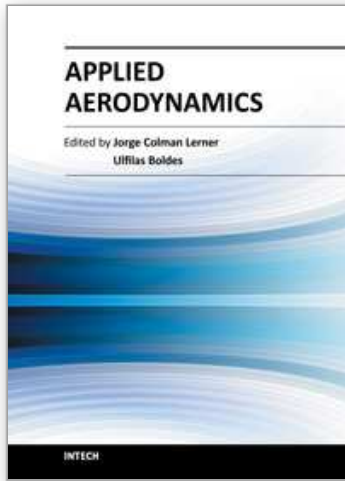
Applied Aerodynamics

Edited by Dr. Jorge Colman Lerner

Aerodynamics, from a modern point of view, is a branch of physics that study physical laws and their applications, regarding the displacement of a body into a fluid, such concept could be applied to any body moving in a fluid at rest or any fluid moving around a body at rest. This Book covers a small part of the numerous cases of stationary and non stationary aerodynamics; wave generation and propagation; wind energy; flow control techniques and, also, sports aerodynamics. It's not an undergraduate text but is thought to be useful for those teachers and/or researchers which work in the several branches of applied aerodynamics and/or applied fluid dynamics, from experiments procedures to computational methods.

How to reference

In order to correctly reference this scholarly work, feel free to copy and paste the following:

Efstathios Konstantinidis and Demetri Bouris (2012). Bluff Body Aerodynamics and Wake Control, Applied Aerodynamics, Dr. Jorge Colman Lerner (Ed.), ISBN: 978-953-51-0611-1, InTech, Available from: http://www.intechopen.com/books/applied-aerodynamics/bluff-body-aerodynamics-and-wake-control

INTECH
open science | open minds